Chemical Science

ROYAL SOCIETY OF CHEMISTRY

EDGE ARTICLE

View Article Online
View Journal | View Issue

Cite this: *Chem. Sci.*, 2021, **12**, 15382

All publication charges for this article have been paid for by the Royal Society of Chemistry

Unexpected high selectivity for acetate formation from CO_2 reduction with copper based 2D hybrid catalysts at ultralow potentials†

Rongming Cai,[ab] Mingzi Sun,[c] Jiazheng Ren,[a] Min Ju,[a] Xia Long,*[a] Bolong Huang*[c] and Shihe Yang*[ab]

Received 3rd October 2021
Accepted 6th November 2021

DOI: 10.1039/d1sc05441d

rsc.li/chemical-science

Copper-based catalysts are efficient for CO_2 reduction affording commodity chemicals. However, Cu(I) active species are easily reduced to Cu(0) during the CO_2RR, leading to a rapid decay of catalytic performance. Herein, we report a hybrid-catalyst that firmly anchors 2D-Cu metallic dots on F-doped Cu_xO nanoplates (Cu_xOF), synthesized by electrochemical-transformation under the same conditions as the targeted CO_2RR. The as-prepared Cu/Cu_xOF hybrid showed unusual catalytic activity towards the CO_2RR for CH_3COO^- generation, with a high FE of 27% at extremely low potentials. The combined experimental and theoretical results show that nanoscale hybridization engenders an effective s,p-d coupling in Cu/Cu_xOF, raising the d-band center of Cu and thus enhancing electroactivity and selectivity for the acetate formation. This work highlights the use of electronic interactions to bias a hybrid catalyst towards a particular pathway, which is critical for tuning the activity and selectivity of copper-based catalysts for the CO_2RR.

Introduction

The electrocatalytic reduction of CO_2 (CO_2RR) with low-cost catalysts holds great promise as a viable CO_2 fixation process.[1,2] Among the catalysts that have been extensively investigated so far, copper is unique in that it is the only metal with a negative adsorption energy for *CO but a positive adsorption energy for *H, favoring the formation of CO_2RR products beyond CO*.[3,4] In recent years, various Cu-based electrocatalysts have been developed including metallic Cu and Cu alloys, as well as Cu compounds,[5,6] and their catalytic performance has been continuously improved by surface faceting, nanostructuring, doping, *etc.*[7–15] It is now widely accepted that the oxidation states of Cu have significant effects on the products of the CO_2RR. For instance, metallic Cu is found to produce CO and HCOOH as the main products at low overpotentials but CH_4 or C_2H_4 at higher overpotentials. For Cu_2O, on the other hand, CH_3OH is the dominant product,[16] and the catalytic activity of Cu_2O decreases quickly due to the decomposition of Cu_2O to Cu.

Several approaches have been reported to stabilize Cu(I) species, such as introduction of the copper nitride (Cu_3N) support,[17,18] electro-redeposition of catalysts,[19,20] and doping.[7] Moreover, the electronic and the crystalline structures of Cu compounds with multiple-anions could be greatly modulated by different charges, ionic radii and electronegativities of anions,[21] leading to different catalytic performances. In fact, it has been shown theoretically and experimentally that the modulation of surface Cu(I) active sites on copper based catalysts with non-metal elements could improve the selectivity of C_2 products by changing the reaction pathways.[8,9,11,22] More recently, hybrid catalysts of Cu(0) and Cu(I) synthesized by electrochemical treatment of physically mixed Cu and CuI powder were found to enhance CO_2 reduction and C–C coupling to generate alcohols.[10,23] However, important information on active sites and effects of anions on catalytic activity and selectivity of hybrid catalysts is still largely missing, hindering the design of efficient CO_2RR catalysts by tailoring their surface/interface properties.

Herein, we report the synthesis and the unusual CO_2RR activity/selectivity of a novel two-dimensional (2D) copper-based hybrid catalyst featuring distinctive F^- anion coordination. First, we systematically investigated the chemical and structural transformation of the 2D Cu(OH)F precursor into the hybrid catalyst under the same conditions as those for the alkaline CO_2RR (Fig. 1A). The introduction of F not only afforded the exposed high energy facets of 2D Cu(0) that were well dispersed

[a]Guangdong Provincial Key Lab of Nano-Micro Material Research, School of Chemical Biology and Biotechnology, Shenzhen Graduate School, Peking University, Shenzhen 518055, China. E-mail: xialong@pku.edu.cn; chsyang@pku.edu.cn

[b]Institute of Biomedical Engineering, Shenzhen Bay Laboratory, Shenzhen 518107, China

[c]Department of Applied Biology and Chemical Technology, The Hong Kong Polytechnic University, Hung Hom, Kowloon, Hong Kong SAR, China. E-mail: bhuang@polyu.edu.hk

† Electronic supplementary information (ESI) available: Experimental details, characterization and performance data of this work. See DOI: 10.1039/d1sc05441d

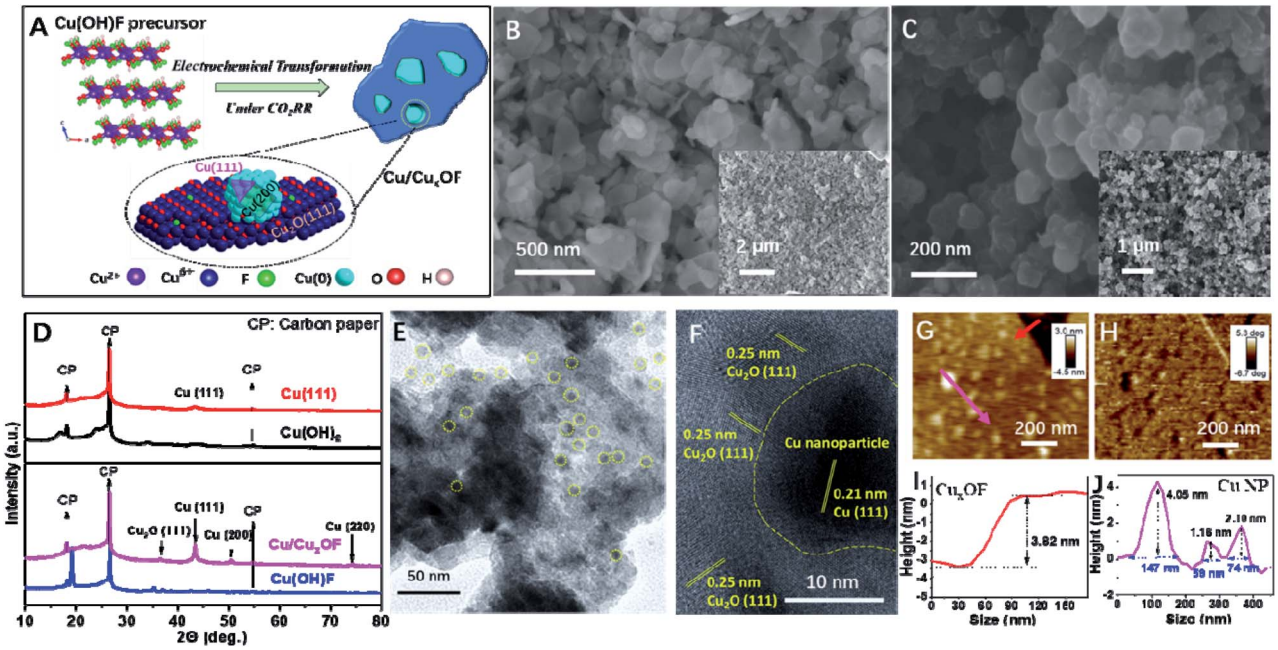

Fig. 1 Morphology and structural characterization of the as-prepared copper hybrid catalyst. (A) Schematic atomic structures of Cu(OH)F and the transformed Cu/Cu_xOF hybrid. (B and C) SEM images of (B) Cu(OH)F precursor and (C) as-formed Cu/Cu_xOF. (D) XRD patterns of Cu(OH)F and $Cu(OH)_2$, and the corresponding transformed copper catalysts of Cu/Cu_xOF and Cu-(111). (E) TEM image and (F) high resolution TEM image of Cu/Cu_xOF. (G–J) AFM height image (G) and the corresponding height profiles of Cu_xOF nanoplates (I) and metallic Cu nanoparticles (J), as well as the AFM phase image (H).

on 2D Cu_xOF (named Cu/Cu_xOF), but also played a critical role in protecting Cu(I) from being fully reduced to Cu(0) under the reductive CO_2RR conditions. Secondly, the highly active sites allowed the as-formed Cu/Cu_xOF to catalyze the CH_3COO^- formation *via* the CO_2RR at an extremely low potential of −0.3 V (*vs.* RHE), outperforming most of the electrocatalysts reported to date for this reaction.[24–27] In combination with theoretical calculations, we revealed the importance of the electronic interaction in terms of the s,p-d coupling between the Cu species and the hetero-anions in promoting the activity/selectivity towards the acetate formation *via* the CO_2RR.

Results and discussion

The Cu(OH)F precursor was synthesized *via* a modified hydrothermal method reported previously,[28] and turned out to be a well crystallized 2D compound according to the XRD patterns (Fig. S1†) and the SEM (Fig. S2† and 1B), TEM and HRTEM (Fig. S3†) images. More interestingly, the 2D microstructure was well-retained after the formation of Cu/Cu_xOF *via* electrochemical transformation, although the surface showed signs of roughening (Fig. 1C). Fig. S4† shows the elemental mapping image from energy dispersive X-ray analysis (EDX), and a uniform distribution of Cu, O and F can be observed. From the X-ray diffraction (XRD) pattern of Cu/Cu_xOF (Fig. 1D), typical diffraction peaks of both Cu_2O and metallic Cu are observed. Apart from the strong diffraction peaks of Cu (111), other smaller peaks corresponding to (200) and (220) were also observed. Importantly, on the larger 2D nanoplates with lateral sizes of several hundreds of nanometers, there lay much smaller ones with sizes of 20–50 nm as found in the transmission electron microscopy (TEM, Fig. 1E, S5 and Table S1†), high resolution TEM (HRTEM, Fig. 1F) and atomic force microscopy (AFM, Fig. 1G–J and S6†) images. Such an overall morphology of Cu/Cu_xOF is illustrated in Fig. 1A. The lattice fringes of ~0.25 nm, ~0.18 nm and 0.21 nm in the HRTEM images (Fig. 1F and S7†) further suggest that the larger nanoplates are made of Cu_2O with the lattice fringe of (111), and the smaller 2D nanoparticles are actually metallic Cu with the lattice fringes of (200) and (111), respectively, in accordance with the XRD results. Note that the as-formed Cu_xOF nanoplates comprise both well crystallized Cu_2O grains and amorphous regions, which could be well distinguished from each other in the HRTEM images (Fig. 1F and S8†). This is also consistent with the low peak intensity of Cu_2O in the XRD patterns (Fig. 1D).

In a control experiment, we also investigated the structural change of Cu(OH)F in 1 M KOH electrolyte, as opposed to the abovementioned electrochemical transformation. From the XRD patterns shown in Fig. S9,† one can see that after the KOH treatment, Cu(OH)F was transformed into $Cu(OH)_2$ with a typical nanowire microstructure (Fig. S10 and S11†). This is supported by the greatly reduced content of F (~0.24%, see Fig. S12†). Of note, the much higher F content in Cu/Cu_xOF is probably due to the fast transformation process as confirmed by *in situ* electrochemical quartz crystal microbalance with dissipation (EQCM-D) (Fig. S13†). These results indicate that the direct electrochemical treatment was the main driving force for the successful formation of Cu/Cu_xOF (with the F content as

high as ~5.92%) from the Cu(OH)F precursor (Fig. S14†). Further, $Cu(OH)_2$ without any F (Fig. S15†) and KOH-treated Cu(OH)F (with ~0.24% F) were subsequently treated under the CO_2RR conditions. As can be seen from the XRD patterns (Fig. 1D and S16†), HRTEM (Fig. S17 and S18†) and AFM (Fig. S19†) images, only 2D metallic Cu(0) with the low-energy facet of (111) could be obtained (named Cu-(111)) from the $Cu(OH)_2$ precursor, while Cu/Cu_xO could be formed by using the KOH-treated Cu(OH)F as the precursor, further confirming the critical role of F in stabilizing the oxidized Cu species.

Then X-ray photoelectron spectroscopy (XPS), Auger electron spectroscopy (AES), and electron paramagnetic resonance (EPR) spectroscopy were combined to get full information on the electronic structure of the metal and anions in the as-prepared copper catalysts. First, the XPS peak of F in Cu/Cu_xOF was much sharper than that of the Cu(OH)F precursor (Fig. 2A), suggesting a different electronic environment of F in Cu/Cu_xOF arising from the decreased content of F and the absence of H^+ ions. The binding energy of O 1s in Cu/Cu_xOF was slightly larger than that in $Cu(OH)_2$ while smaller than that in Cu(OH)F (Fig. 2B), signifying the electron withdrawing and polarization effects of F on O 1s, and expectedly, on the directly bonded metal ions, *i.e.*, $Cu^{\delta+}$.[29] Moreover, negligible peaks could be found for the O spin-orbital of Cu-(111) (Fig. S20†), indicating the existence of only metallic Cu without any oxidized copper species, in accordance with the results of XRD (Fig. 1D), HRTEM (Fig. S17†) and XPS of Cu-(111) in the Cu 2p spin-orbital (Fig. 2C). As expected, for the $Cu(OH)_2$ precursor, Cu^{2+} located at 935.5 eV was clearly observed. Notably, a large positive shift of Cu 2p was observed for Cu(OH)F (Fig. S21†) due to the strong polarization and electron withdrawing effects of F as mentioned above. For the as-prepared Cu/Cu_xOF, however, we found that besides Cu(0), there also existed moieties between Cu(0) and Cu(I), hereafter denoted as $Cu^{\delta+}$ (to distinguish them from Cu and Cu(I) in Cu_2O), as shown in Fig. 2C, D and S22.† The LMM Auger spectra of copper shown in Fig. 2E further confirm the existence of metallic Cu(0) and $Cu^{\delta+}$ in the as-prepared Cu/Cu_xOF. These results suggest that in addition to the electronic interactions between O and F, the two anions together also impact the Cu species, and thus would influence the catalytic performance of the hybrid catalyst.

Further, EPR spectra were collected and analyzed in order to get detailed information on the unpaired electrons in the material. The *g*-factor is a dimensionless measure of the intrinsic magnetic moments of the electron, which is 2.0023 for a free electron but can vary for unpaired electrons in different molecules and materials. Here Cu(I) has a d^{10} electronic configuration with no unpaired electrons and thus is EPR silent. However, EPR is a useful tool for both structural and mechanistic studies of Cu(II) and Cu(0) on account of their d^9 and $d^{10}s^1$ configurations, respectively. As can be seen from Fig. S23,† Cu-(111) and Cu/Cu_xOF show a *g* value close to ~2.63, indicating the presence of unpaired electrons in both the materials of similar origin, namely the metallic Cu species.

We examined the stability of the catalysts by checking any possible structural changes. As shown in Fig. 2F, all the XPS peaks for F, O, and Cu spin-orbitals of Cu/Cu_xOF showed a negligible change after the electrochemical CO_2RR evaluation

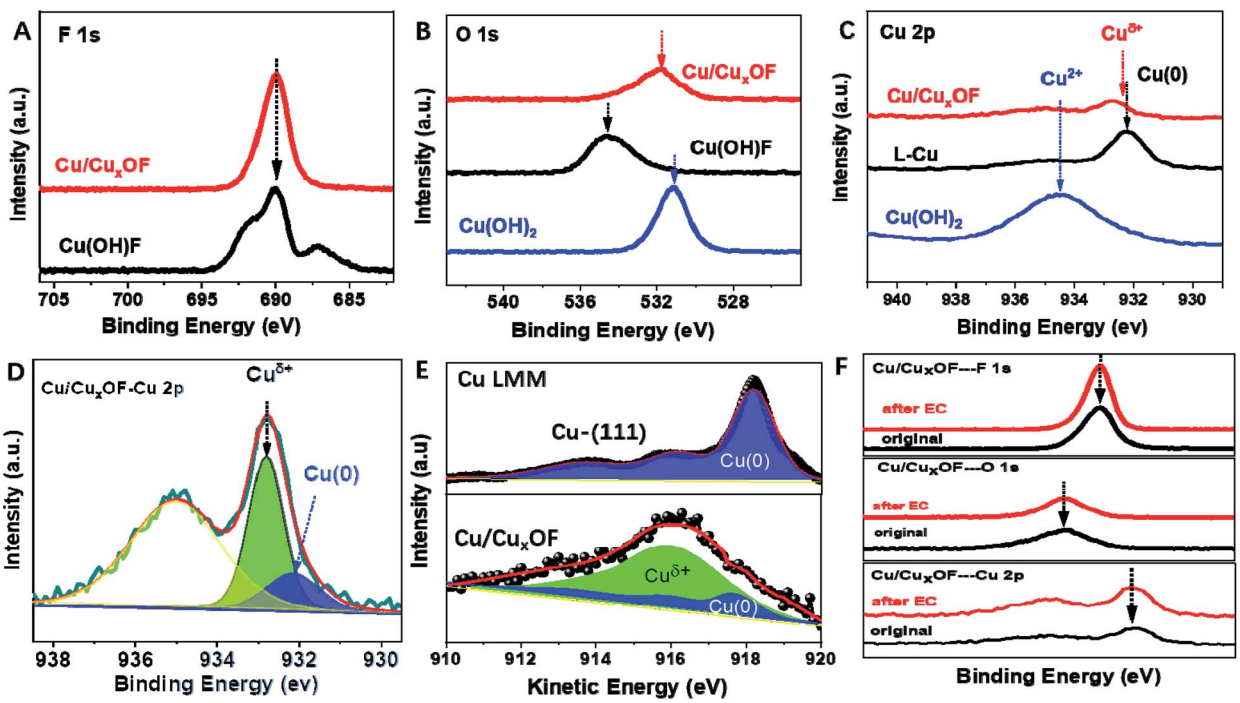

Fig. 2 XPS analysis of the copper catalysts and precursors. (A) F 1s of Cu/Cu_xOF and the Cu(OH)F precursor, (B) O 1s of Cu/Cu_xOF, the Cu(OH)F precursor and $Cu(OH)_2$ precursor, (C) Cu 2p of Cu/Cu_xOF, Cu-(111) and the $Cu(OH)_2$ precursor, (D) de-convoluted XPS spectrum of Cu 2p for Cu/Cu_xOF, (E) Cu LMM Auger spectra of Cu/Cu_xOF and Cu-(111), and (F) comparison of the XPS spectra of Cu/Cu_xOF at F 1s, O 1s, and Cu 2p spin-orbitals before and after the electrochemical tests at the stepped potentials from −0.3 V to −0.7 V *vs.* RHE for more than 28 h.

at the stepped potentials from −0.3 V to −0.7 V *vs.* RHE for more than 28 h. Moreover, based on the XRD (Fig. S24†), TEM (Fig. S25†), HRTEM (Fig. S26†) and elemental analysis (Fig. S27 & S28†) results, we found that both the metallic Cu and 2D Cu_xOF with ∼5.83% of F (close to the initial value of ∼5.92%) were retained after the ∼28 h stability tests, indicating the good working stability of the as-prepared Cu/Cu_xOF for the CO_2RR. In addition, the *in situ* EQCM-D further suggests that the surface of Cu/Cu_xOF is actually in a dynamic equilibrium as characterized by periodic adsorption–desorption processes during the CV cycles (Fig. S29†).[30,31]

Then we proceeded to the electrochemical performance of the as-prepared copper catalysts towards the CO_2RR, which was evaluated in a flow cell with 1 M KOH as the electrolyte (see the ESI† for details). From the *J*–*V* curves (Fig. 3A), it is clear that Cu/Cu_xOF showed larger current densities than Cu-(111) and Cu/Cu_xO at the same applied potentials. Moreover, the partial current density (Fig. S30†) and faradaic efficiency (FE, Fig. 3B) of CH_3COO^- on Cu/Cu_xOF were found to be ∼4.0 mA cm^{-2} and 27% at a low potential of −0.3 V (*vs.* RHE), which differs from those of the main C_2 products of C_2H_5OH and C_2H_4 on Cu-(111) (Fig. S31†) and Cu/Cu_xO (Fig. S32†), and also competes with the best noble-metal free electrocatalysts for the CO_2RR with the selective product of CH_3COO^- that usually required more negative potentials (Table S2†).[16,24–27,32] We noted that Cu/Cu_xOF and Cu/Cu_xO have a similar microstructure including both nanoparticle size and hierarchical structure (Fig. S33–S35†), thus the distinctive catalytic selectivity of Cu/Cu_xOF for the CO_2RR (Fig. 3E–I) probably results from the F-doping induced modification of surface physicochemical properties of Cu/Cu_xOF, which would favor the acetate formation. Moreover, the current density of the CO_2RR reached ∼56 mA cm^{-2} at E = −0.5 V (*vs.* RHE) (Fig. 3A), larger than the reported values collected on copper based catalysts under similar reaction conditions.[13,33,34] In addition, compared with Cu-(111) and Cu/Cu_xO, Cu/Cu_xOF showed much higher FE for the CO_2RR (Fig. 3C) and lower FE for the HER (Fig. 3D) in the whole potential range from −0.3 to −0.7 V *vs.* RHE, demonstrating much better CO_2RR activity of Cu/Cu_xOF than Cu-(111) and Cu/Cu_xO catalysts. The long-term stability at stepped potentials was also estimated. From Fig. S36,† it is clear that the change of the CO_2RR current density at each stage is less than 5% even at a deep potential down to −0.7 V *vs.* RHE. What's more, the FE of acetate during the stability tests was essentially unchanged at each potential, evidencing the good catalytic stability of the as-prepared Cu/Cu_xOF for the CO_2RR. In conjunction with the structural stability discussed earlier in the previous paragraph, we can conclude that the as-prepared Cu/Cu_xOF is indeed an advanced electrocatalyst for the CO_2RR with excellent catalytic selectivity and stability toward acetate generation.

As is widely known, the CO_2RR involves multiple electron-transfer and chemical reaction steps, and this complex process strongly depends on the physiochemical and surface properties of the catalysts. Previous theoretical and experimental studies have demonstrated that the products of the CO_2RR at low overpotentials were generally limited to C_1 species on metallic Cu nanocatalysts, especially on their low-energy facets, such as CO and HCOOH.[35,36] This was in accordance with the results observed for Cu-(111) prepared in this work. At high potentials, the FE of C_2 increased along with the suppression of the HER, which again agrees with what we observed for Cu-(111) (Fig. 3G, I and S37†).[37,38] However, markedly different catalytic selectivities were observed for Cu/Cu_xOF. Specifically, the FE of C_2 products was maintained at ∼30% in almost the whole potential range we studied, while the FE of C_1 products increased (Fig. 3G and F) in parallel with the

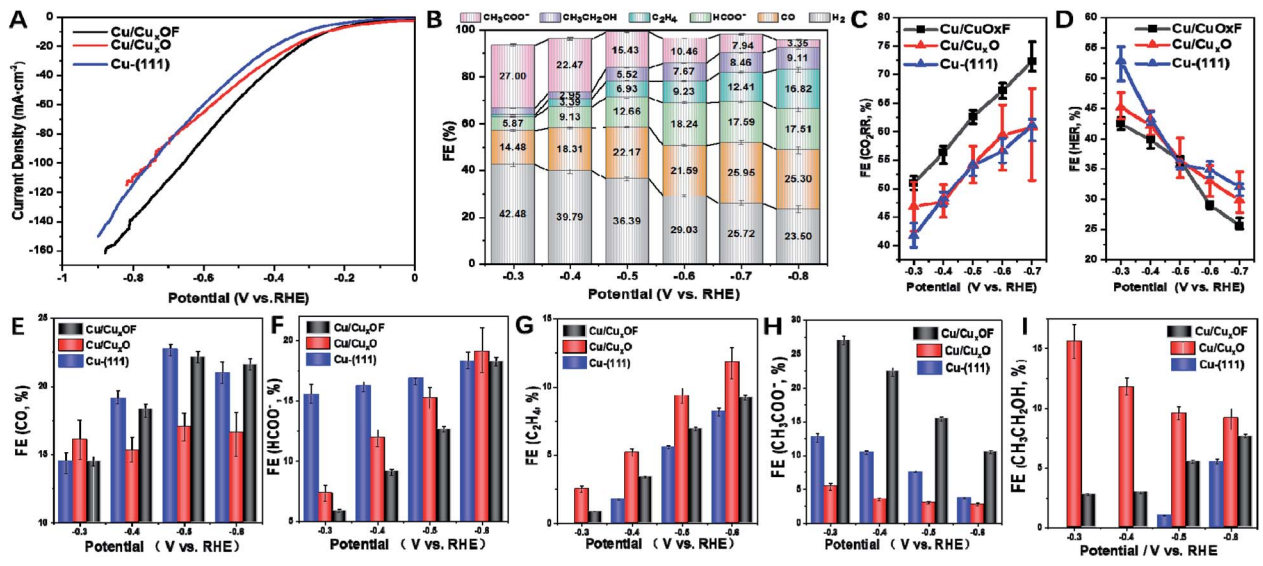

Fig. 3 Electrocatalytic performance towards the CO_2RR in 1 M KOH. (A) *J*–*V* curves collected on Cu-(111), Cu/Cu_xO and Cu/Cu_xOF. (B) FE of all the products on Cu/Cu_xOF at various applied potentials. (C and D) FE for (C) the CO_2RR and (D) HER on Cu-(111), Cu/Cu_xO and Cu/Cu_xOF. (E–I) comparison of FE on Cu-(111), Cu/Cu_xO and Cu/Cu_xOF for all the CO_2RR products of (E) CO, (F) $HCOO^-$, (G) C_2H_4, (H) CH_3COO^- and (I) CH_3CH_2OH.

suppression of the HER when the applied potential increased (Fig. 3E–I), amounting to ~72% FE at −0.7 V *vs.* RHE (Fig. 3B and C). So what is the explanation for this striking catalytic performance? Plausibly, in Cu/Cu$_x$OF with F-coordination, multi-copper oxidation states and the hierarchical 2D–2D microstructure, could provide multiple sites with different adsorption–desorption characteristics for the reactants and intermediates of the CO_2RR (Scheme S1†), promoting C–C coupling[9,39–41] to form the CH_3COO^- product even at very low overpotentials. More detailed discussions on the reaction mechanism along with theoretical calculations will be provided below.

To better understand the CO_2RR process on the copper-based hybrid catalysts, we carried out the DFT calculations of their electronic structures and energy trends in the reaction process of interest here, and then explored the effects of the electronic structure and energy on electroactivity of the catalysts (Fig. S38†). Clearly, the Cu-(111) surface shows a highly ordered electronic distribution guided by the Cu sites (Fig. 4A). Such a surface electronic structure usually leads to low product selectivity due to the strong competition between different reaction pathways. By contrast, the Cu/Cu$_x$OF surface shows a strong perturbation of the electronic distribution near the Fermi level (E_F) (Fig. 4B) due to hybridization with the Cu$_x$OF nanoplate. We believe that the resulting strong bonding orbitals of the metallic Cu nanoparticle surfaces played an important role in forming the highly electroactive region for the CO_2RR. To illustrate this point more clearly on Cu/Cu$_x$OF, Fig. 4C displays the projected partial density of states (PDOS). Notably, the Cu-3d orbitals in Cu/Cu$_x$OF are now located at a position much closer to the E_F than those in Cu-(111), meaning a higher d-band center and thus an improved electroactivity. Meanwhile, both the O-s,p, and the F-s,p orbitals are located deeper in energy, which acted as the electron reservoir. Compared to Cu/Cu$_x$OF, Cu/Cu$_x$O shows a slightly lower d-band center, which leads to decreased electroactivity and FE of the C_2 products (Fig. S39†).

We next unravel the site-dependent PDOS of the different elements in the catalysts. Focusing now on the Cu sites, we notice that from the bulk Cu$_x$OF nanoplate to the surface of metallic Cu with high-energy facets, Cu-3d orbitals exhibited a nearly linear upshifting trend toward the E_F (Fig. 4D). Consequently, the surface Cu nanoparticles with high electroactivity were found to be the active sites for the CO_2RR process. Then, the electronic structures of both O and F sites in the Cu$_x$OF

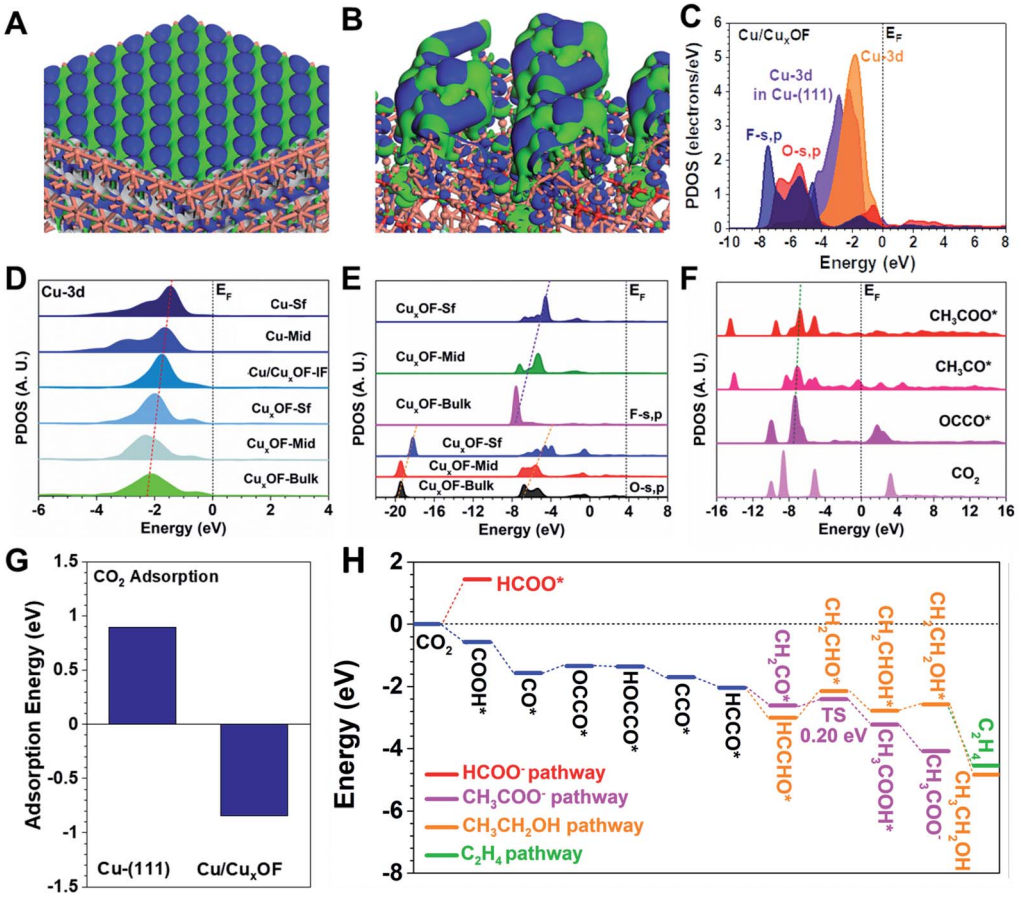

Fig. 4 The 3D contour plot for electronic distributions of (A) Cu-(111) and (B) Cu/Cu$_x$OF. (C) PDOS of Cu/Cu$_x$OF. Site-dependent PDOS of (D) Cu-3d, and (E) O-s,p and F-s,p in Cu/Cu$_x$OF. (F) The PDOS of key adsorbates during the CO_2RR process. (G) The comparison of CO_2 adsorption on Cu-(111) and Cu/Cu$_x$OF. (H) The CO_2RR reaction pathways on Cu/Cu$_x$OF. The orange, red, and cyan balls in (A) and (B) represent Cu, O and F atoms, respectively, and the blue and green isosurfaces indicate the bonding and anti-bonding orbitals, respectively. The dashed lines in (D and E) represent the higher position of the band centers for Cu and O-s,p, and F-s,p, respectively.

nanoplates are investigated (Fig. 4E). Notably, from the bulk to the nanoplate surface, the s,p orbitals exhibit a gradual upshifting trend, which supports the improved electron transfer capability from the Cu_xOF surface to the Cu nanoparticle surface, and ultimately to the intermediates during the CO_2RR. To follow up the intermediate conversion process, the PDOS of key adsorbates during the CO_2RR process are displayed in Fig. 4F. The structural configurations of these key adsorbates are displayed in Fig. S40.† Compared to the free CO_2, the s,p orbitals of the intermediates have shown a slight upshift, confirming the successful reduction of CO_2. In the reduction of OCCO* to CH_3COO*, we notice a nearly linear correlation of the s,p orbital energies, a sign that would guarantee efficient electron transfer and the intermediate conversions. The linear correlation of the σ orbitals with an upshifting trend is well preserved, which not only indicates the most efficient electron transfer but also the optimal adsorption strength of intermediates for the CO_2RR.

Finally, the adsorption of CO_2 on the catalysts was also investigated. Compared to the Cu-(111) surface, the adsorption on Cu/Cu_xOF became much more energetically favorable (Fig. 4G). While the CO_2 adsorption on the Cu-(111) surface showed an energy cost as high as 0.89 eV, Cu/Cu_xOF demonstrates a highly exothermic adsorption energy of −0.84 eV, accounting for the high electroactivity towards the CO_2RR. The energy evolution of the CO_2RR process is shown in Fig. 4H. For the initial hydrogenation, the strong preference of O–H over C–H shows a low selectivity towards the formation of $HCOO^-$ on Cu/Cu_xOF. The key reaction step in formation of C_2 products usually relies on the coupling of the CO* intermediates to form OCCO*, which shows only a minor energy barrier of 0.22 eV. The following reduction steps are all energetically favorable until the formation of HCCO*. In further hydrogenation, the formation of both CH_2CO* and HCCHO* becomes exothermic. The key step in acetic acid formation is the incorporation of water in CH_2CO*, which is energetically favorable with a small activation barrier of 0.20 eV. This low barrier guarantees the efficient conversion towards CH_3COOH*. Remarkably, the strong reaction trend with an energy release of −4.08 eV makes the formation of CH_3COO^- the most preferred of all the reaction pathways at a very low potential, in good agreement with the foregoing experimental findings. Proceeding with the CH_3CH_2OH and C_2H_4 reaction pathways, the hydrogenation steps from HCCHO* to CH_2CHO* and from CH_2CHOH* to CH_2CH_2OH* have an energy barrier of 0.87 and 0.22 eV, respectively. These substantial energy barriers, especially the first one, largely limit the formation of both CH_3CH_2OH and C_2H_4 at low potentials. However, by increasing the applied potential, the contents of CH_3CH_2OH and C_2H_4 will gradually increase, as we observed experimentally. Therefore, both electronic structures and reaction trends have confirmed the high electroactivity and selectivity of Cu/Cu_xOF towards the generation of C_2 products during the CO_2RR.

Conclusions

In summary, by exploiting 2D Cu(OH)F nanoplates as a precursor, we successfully synthesized a copper based hybrid catalyst, by coupling 2D metallic Cu nanoparticles with high-energy facets and F-doped Cu_xO (Cu_xOF) nanoplates. For the catalyst synthesis with *in situ* electrochemical transformation, we purposely used the same conditions as those for the alkaline CO_2RR in order to ensure a durable catalytic operation. The critical roles of F-modification have been revealed to effectively tailor the exposed facets of metallic Cu nanoparticles, stabilize the oxidized copper active species under the CO_2RR conditions, and more importantly, to purposely induce the s,p-d coupling between the metal and hetero-anions tending heavily towards the acetate pathway. Consequently, the as-prepared 2D Cu/Cu_xOF hybrid catalyst creates an electronic environment leading to high electroactivity, particularly the unexpected CH_3COO^- selectivity at an extremely low overpotential. This work unravels interesting electronic interactions between Cu species and different anions in copper-based hybrid materials, and provides an efficient strategy to construct more efficient catalysts for the CO_2RR.

Data availability

All experimental and computational data are available within the article or in the ESI file.†

Author contributions

X. L. and S. Y. conceived the idea. R. C. synthesized the catalysts. R. C. and J. R. carried out structural and electrochemical characterization. R. C. and X. L. performed EQCM-D experiments. R. C., M. J. and X. L. performed AFM characterization experiments. R. C., M. J., and J. R. performed morphology characterization. X. L. and R. C. prepared the figures and analyzed the data. M. S. and B. H. performed the DFT calculations. X. L., R. C. B. H. and S. Y. wrote the manuscript. All the authors discussed the results and commented on the manuscript at all stages.

Conflicts of interest

There are no conflicts to declare.

Acknowledgements

The authors appreciate the financial support from the National Natural Science Foundation of China (21703003, and 21972006), Shenzhen Peacock Plan (KQTD2016053015544057), Shenzhen Science and Technology Innovation Commission (JCYJ20180302153417057, and JCYJ20190808155413194), and Nanshan Pilot Plan (LHTD20170001).

Notes and references

1 R. Cai, M. Ju, J. Chen, J. Ren, J. Yu, X. Long and S. Yang, *Mater. Chem. Front.*, 2021, **5**, 3576–3592.
2 Y. Liu, S. Chen, X. Quan and H. Yu, *J. Am. Chem. Soc.*, 2015, **137**, 11631–11636.
3 A. Bagger, W. Ju, A. S. Varela, P. Strasser and J. Rossmeisl, *ChemPhysChem*, 2017, **18**, 3266–3273.

4 S. Nitopi, E. Bertheussen, S. B. Scott, X. Liu, A. K. Engstfeld, S. Horch, B. Seger, I. E. L. Stephens, K. Chan, C. Hahn, J. K. Norskov, T. F. Jaramillo and I. Chorkendorff, *Chem. Rev.*, 2019, **119**, 7610–7672.
5 M. B. Gawande, A. Goswami, F. X. Felpin, T. Asefa, X. Huang, R. Silva, X. Zou, R. Zboril and R. S. Varma, *Chem. Rev.*, 2016, **116**, 3722–3811.
6 D. Raciti and C. Wang, *ACS Energy Lett.*, 2018, **3**, 1545–1556.
7 Y. Zhou, F. Che, M. Liu, C. Zou, Z. Liang, P. De Luna, H. Yuan, J. Li, Z. Wang, H. Xie, H. Li, P. Chen, E. Bladt, R. Quintero-Bermudez, T. K. Sham, S. Bals, J. Hofkens, D. Sinton, G. Chen and E. H. Sargent, *Nat. Chem.*, 2018, **10**, 974–980.
8 M. B. Ross, P. De Luna, Y. F. Li, C. T. Dinh, D. Kim, P. Yang and E. H. Sargent, *Nat. Catal.*, 2019, **2**, 648–658.
9 H. Mistry, A. S. Varela, C. S. Bonifacio, I. Zegkinoglou, I. Sinev, Y. W. Choi, K. Kisslinger, E. A. Stach, J. C. Yang, P. Strasser and B. R. Cuenya, *Nat. Commun.*, 2016, **7**, 12123.
10 H. Xiao, W. A. Goddard III, T. Cheng and Y. Liu, *Proc. Natl. Acad. Sci. U. S. A.*, 2017, **114**, 6685–6688.
11 F. L. Ni, H. Yang, Y. Z. Wen, H. P. Bai, L. S. Zhang, C. Y. Cui, S. Y. Li, S. S. He, T. Cheng, B. Zhang and H. S. Peng, *Sci. China Mater.*, 2020, **63**, 2606–2612.
12 K. Sun, T. Cheng, L. Wu, Y. Hu, J. Zhou, A. Maclennan, Z. Jiang, Y. Gao, W. A. Goddard III and Z. Wang, *J. Am. Chem. Soc.*, 2017, **139**, 15608–15611.
13 J. J. Lv, M. Jouny, W. Luc, W. Zhu, J. J. Zhu and F. Jiao, *Adv. Mater.*, 2018, **30**, e1803111.
14 E. Landaeta, R. A. Masitas, T. B. Clarke, S. Rafacz, D. A. Nelson, M. Isaacs and Z. D. Schultz, *ACS Appl. Nano Mater.*, 2020, **3**, 3478–3486.
15 X. Yang, E. A. Fugate, Y. Mueanngern and L. R. Baker, *ACS Catal.*, 2017, **7**, 177–180.
16 M. Le, M. Ren, Z. Zhang, P. T. Sprunger, R. L. Kurtz and J. C. Flake, *J. Electrochem. Soc.*, 2011, **158**, E45–E49.
17 Z. Y. Yin, C. Yu, Z. L. Zhao, X. F. Guo, M. Q. Shen, N. Li, M. Muzzio, J. R. Li, H. Liu, H. H. Lin, J. Yin, G. Lu, D. Su and S. H. Sun, *Nano Lett.*, 2019, **19**, 8658–8663.
18 C. Giordano and M. Antonietti, *Nano Today*, 2011, **6**, 366–380.
19 D. Wakerley, S. Lamaison, F. Ozanam, N. Menguy, D. Mercier, P. Marcus, M. Fontecave and V. Mougel, *Nat. Mater.*, 2019, **18**, 1222–1227.
20 W. C. Ma, S. J. Xie, T. T. Liu, Q. Y. Fan, J. Y. Ye, F. F. Sun, Z. Jiang, Q. H. Zhang, J. Cheng and Y. Wang, *Nat. Catal.*, 2020, **3**, 478–487.
21 H. Kageyama, K. Hayashi, K. Maeda, J. P. Attfield, Z. Hiroi, J. M. Rondinelli and K. R. Poeppelmeier, *Nat. Commun.*, 2018, **9**, 772.
22 S. Popovic, M. Smiljanic, P. Jovanovic, J. Vavra, R. Buonsanti and N. Hodnik, *Angew. Chem., Int. Ed.*, 2020, **59**, 14736–14746.
23 H. Li, T. Liu, P. Wei, L. Lin, D. Gao, G. Wang and X. Bao, *Angew. Chem., Int. Ed.*, 2021, **60**, 14329–14333.
24 K. P. Kuhl, E. R. Cave, D. N. Abram and T. F. Jaramillo, *Energy Environ. Sci.*, 2012, **5**, 7050–7059.
25 C. Genovese, M. E. Schuster, E. K. Gibson, D. Gianolio, V. Posligua, R. Grau-Crespo, G. Cibin, P. P. Wells, D. Garai, V. Solokha, S. K. Calderon, J. J. Velasco-Velez, C. Ampelli, S. Perathoner, G. Held, G. Centi and R. Arrigo, *Nat. Commun.*, 2018, **9**, 935.
26 Y. M. Liu, S. Chen, X. Quan and H. T. Yu, *J. Am. Chem. Soc.*, 2015, **137**, 11631–11636.
27 Y. Wang, D. G. Wang, C. J. Dares, S. L. Marquard, M. V. Sheridan and T. J. Meyer, *Proc. Natl. Acad. Sci. U. S. A.*, 2018, **115**, 278–283.
28 H. Tian, Y. Wang, J. Zhang, Y. Ma, H. Cui, Q. Cui and Y. Ma, *J. Phys. Chem. C*, 2019, **123**, 25492–25500.
29 Y. Kawamoto, K. Ogura, M. Shojiya, M. Takahashi and K. Kadono, *J. Fluorine Chem.*, 1999, **96**, 135–139.
30 N. Shpigel, M. D. Levi, S. Sigalov, O. Girshevitz, D. Aurbach, L. Daikhin, P. Pikma, M. Marandi, A. Jänes, E. Lust, N. Jäckel and V. Presser, *Nat. Mater.*, 2016, **15**, 570–575.
31 M. Ju, R. Cai, J. Ren, J. Chen, L. Qi, X. Long and S. Yang, *ACS Appl. Mater. Interfaces*, 2021, **13**, 37063–37070.
32 R. N. De, S. Gonglach, S. Paul, M. Haas, S. S. Sreejith, P. Gerschel, U. P. Apfel, T. H. Vuong, J. Rabeah, S. Roy and W. Schofberger, *Angew. Chem., Int. Ed.*, 2020, **59**, 10527–10534.
33 C. T. Dinh, T. Burdyny, M. G. Kibria, A. Seifitokaldani, C. M. Gabardo, F. P. Garcia de Arquer, A. Kiani, J. P. Edwards, P. De Luna, O. S. Bushuyev, C. Zou, R. Quintero-Bermudez, Y. Pang, D. Sinton and E. H. Sargent, *Science*, 2018, **360**, 783–787.
34 T.-T. Zhuang, Y. Pang, Z.-Q. Liang, Z. Wang, Y. Li, C.-S. Tan, J. Li, C. T. Dinh, P. De Luna, P.-L. Hsieh, T. Burdyny, H.-H. Li, M. Liu, Y. Wang, F. Li, A. Proppe, A. Johnston, D.-H. Nam, Z.-Y. Wu, Y.-R. Zheng, A. H. Ip, H. Tan, L.-J. Chen, S.-H. Yu, S. O. Kelley, D. Sinton and E. H. Sargent, *Nat. Catal.*, 2018, **1**, 946–951.
35 F. Calle-Vallejo and M. T. Koper, *Angew. Chem., Int. Ed.*, 2013, **52**, 7282–7285.
36 C. W. Li, J. Ciston and M. W. Kanan, *Nature*, 2014, **508**, 504–507.
37 Y. Yoon, A. S. Hall and Y. Surendranath, *Angew. Chem., Int. Ed.*, 2016, **55**, 15282–15286.
38 A. S. Hall, Y. Yoon, A. Wuttig and Y. Surendranath, *J. Am. Chem. Soc.*, 2015, **137**, 14834–14837.
39 S. Ma, M. Sadakiyo, R. Luo, M. Heima, M. Yamauchi and P. J. A. Kenis, *J. Power Sources*, 2015, **301**, 219–228.
40 A. A. Peterson and J. K. Nørskov, *J. Phys. Chem. Lett.*, 2012, **3**, 251–258.
41 K. J. P. Schouten, Y. Kwon, C. J. M. v. d. Ham, Z. Qin and M. T. M. Koper, *Chem. Sci.*, 2011, **2**, 1902–1909.